Research Square

Preprints are preliminary reports that have not undergone peer review.
They should not be considered conclusive, used to inform clinical practice,
or referenced by the media as validated information.

Evolution of TRi-structural ISOtropic (TRISO) Fuel Material Properties Under Simulated Repository Irradiation Conditions

Shamim Pourrahimi
Western University
Sandeep Kumar Sahni
Western University
Ivan Barker
Western University
Jonas Hedberg
Western University
James J. Noël
Western University
Lyudmila V. Goncharova
Western University
Samantha Michelle Gateman
samantha.gateman@uwo.ca
Western University

Article

Keywords: Alpha Radiation, Gamma Radiation, Deep Geological Repository, TRISO, Ion Implantation, Raman Spectroscopy, X-ray Computed Tomography, Nano-indentation

Posted Date: September 9th, 2026

DOI: https://doi.org/10.21203/rs.3.rs-10822377/v1

License: This work is licensed under a Creative Commons Attribution 4.0 International License.
Read Full License

Additional Declarations: No competing interests reported.

Title: Evolution of TRi-structural ISOtropic (TRISO) Fuel Material Properties Under Simulated Repository Irradiation Conditions

Authors: *Shamim Pourrahimi[1], Sandeep Kumar Sahni[2], Ivan Barker[3], Jonas Hedberg[3], James J. Noël[1,3], Lyudmila V. Goncharova[4*], Samantha Michelle Gateman[1,3*]*

[1]*Department of Chemistry, University of Western Ontario, London, Ontario, Canada*

[2] *Department of Mechanical and Materials Engineering, University of Western Ontario, London, Ontario, Canada*

[3] *Surface Science Western, The University of Western Ontario, London, Ontario, Canada*

[4] *Department of Physics and Astronomy, University of Western Ontario, London, Ontario, Canada*

Corresponding author Lyudmila V. Goncharova: *lgonchar@uwo.ca

Corresponding author Samantha Michelle Gateman: *Samantha.gateman@uwo.ca

Abstract

TRi-structural ISOtropic (TRISO) fuel is a new-generation nuclear fuel with a multilayer coating system for long-term containment. However, the effect of ionizing radiation from radioactive decay on the coupled multilayer system under deep geological repository (DGR) conditions remains insufficiently understood. In this work, we studied the effects of DGR-relevant alpha- and gamma-radiation conditions on pyrolytic carbon (PyC) and silicon carbide (SiC) layers. Raman spectroscopy showed that alpha irradiation caused significant structural changes in both PyC and SiC. Irradiation at 100°C to simulate annealing did not cause noticeable recovery in either material. Nanoindentation results showed increased hardness and elastic modulus after alpha irradiation, whereas gamma irradiation resulted in a softer mechanical response without major chemical changes. The results indicate that the changes may increase the susceptibility of the coating layers to cracking or fracture and are therefore important for understanding the safe long-term containment of TRISO fuel under repository conditions.

Keywords: Alpha Radiation; Gamma Radiation; Deep Geological Repository; TRISO; Ion Implantation; Raman Spectroscopy; X-ray Computed Tomography; Nano-indentation

Introduction

With the growing demand for sustainable energy, nuclear power is receiving renewed attention as a reliable low-carbon energy source. Alongside large-scale reactors operating worldwide, the implementation of small modular reactors (SMRs) is gaining momentum.[1–3] SMRs typically produce up to ~450 MWe and offer compact, modular designs that enable cost-effective, factory-based construction and flexible deployment in remote or grid-constrained regions.[4] As of 2024, China[5] and Russia[6] are using SMRs for power generation, and more than 68 SMR designs are under development or in the licensing process worldwide.[2] To improve fuel containment and enhance reactor safety, seventeen SMR concepts may use TRi-structural ISOtropic (TRISO) coated particles as their nuclear fuel.[7]

A TRISO fuel particle is composed of a fuel kernel surrounded by successive layers of buffer (porous pyrolytic carbon (PyC)), dense inner PyC (IPyC), silicon carbide (SiC), and dense outer PyC (OPyC),[8] as illustrated in Figure 1A. In practical fuel configurations, thousands of TRISO particles are embedded in graphite pebbles or ceramic fuel compacts. This multilayer architecture provides effective confinement of fission products and radionuclides, making TRISO fuel one of the most robust nuclear fuel forms for modern reactor systems under extreme operating and accident reactor conditions.[9,10]

Beyond reactor operation, spent TRISO fuel must remain safely isolated from people and the environment over geological timescales. Disposal in deep geological repositories (DGR), typically at depths of 100-1000 m underground, is widely considered the most viable proposed long-term solution for high-level radioactive waste, and has been adopted as a way forward in many countries, including Canada, Switzerland, Sweden and others.[11] While exact details may be different from one location to another, typically a DGR comprises a series of natural and engineered barriers that includes the mechanically and chemically robust used fuel container (UFC), the repository sealing system, and the geosphere, as schematically shown in Figure 1B.[12]

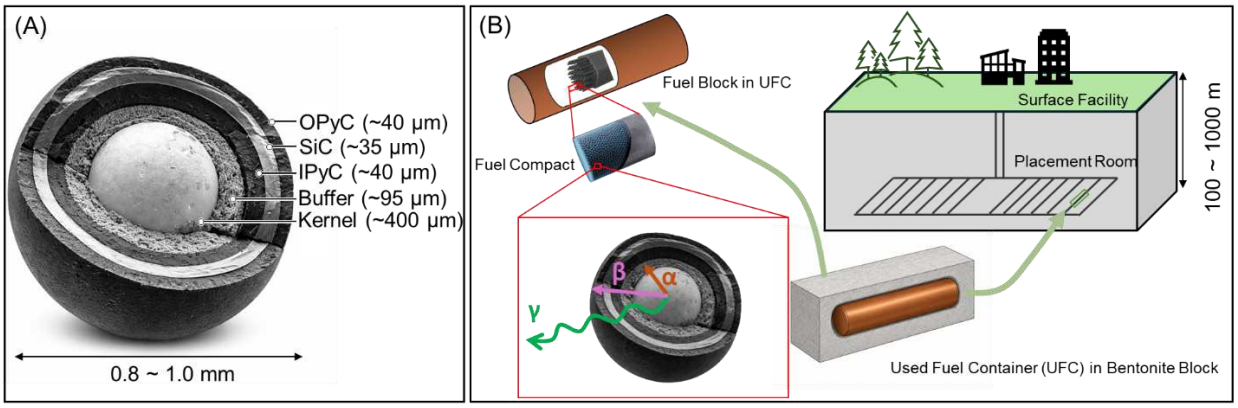


Figure 1: (A) Schematic cutaway image of a single TRISO particle showing the structural design, with approximate kernel diameter and coating layer thicknesses, (B) the multibarrier system design for the Canadian concept of a DGR, as well as penetration depths of different types of ionizing radiation from TRISO particles.

Spent fuel would remain radioactive throughout the proposed lifetime of a DGR, due to the decay of radionuclides with half-lives ranging from days to millions of years, emitting alpha (α), beta (β), and gamma (γ) radiation.[13] The penetration depths of different radiation types from a TRISO kernel are schematically shown in Figure 1B. Few α particles escape the kernel of an intact TRISO particle and all of those are stopped within the first few micrometers of the buffer layer. Most β radiation is absorbed within the combined thickness of the buffer, IPyC, and SiC layers.[14] γ radiation is highly penetrating and can pass through the TRISO particle's overlying coatings and affect other particles and even the metallic container.[15] In repositories, failure scenarios in which the kernel or one of the PyC or SiC layers becomes exposed to the surrounding environment cannot be excluded.[16] In such cases, α radiation may reach TRISO constituent materials and consequently impact their properties. As the radionuclide retention of TRISO particles relies on the structural integrity of the coating layers, it is important to understand how radiation emitted from radioactive decay may alter coating properties over time.

To date, there is limited published research on the influence of α and γ irradiation on TRISO particles. The most directly relevant studies focus on the constituent TRISO materials, particularly SiC and PyC, which are typically investigated separately (often in bulk form) rather than as an integrated, multilayer TRISO structure. [17,18] Ion implantation is widely used to mimic neutron-irradiation damage in reactor fuels and structural materials, and the same concept can be extended

to study α-induced damage.[19] The implantation parameters include the incident ion, energy and dose, which can be adjusted to achieve different levels of damage, measured in displacements per atom (DPA) representing either neutron irradiation in reactors or α irradiation under repository conditions.[20]

For instance, in a study by He et al., Xe ion implantation of PyC to a level of 0.5 DPA caused both chemical and physical changes, including irradiation-induced structural deterioration of the graphitic lattice and increased hardness and elastic modulus. Post-irradiation annealing at 500–1000 °C, representative of reactor operating temperatures, reversed irradiation-induced defects and largely restored the materials' properties.[17] Similar property evolution was observed in a partial TRISO particle consisting of a zirconia kernel coated only with the buffer and IPyC layers, which was irradiated up to 40 DPA to mimic fuel damage accumulated over approximately five years of operation.[18]

The SiC layer in TRISO particles is typically produced by chemical vapor deposition (CVD) as polycrystalline cubic SiC (3C-SiC, often referred to as β-SiC). However, much of the irradiation literature relevant to this topic focuses on single-crystal SiC or 6H-SiC, a hexagonal polytype. For example, Ar^+ implantation of single-crystal and polycrystalline 6H-SiC to a target damage of ~2.6 DPA caused amorphization, leading to a reduction in density and decreased hardness and elastic modulus compared with the unirradiated materials.[21] Similarly, He implantation in the same type of SiC has been reported to cause amorphization. [22] However, amorphization was prevented during implantation at temperatures of 450 to 750 °C, again representative of reactor operation. Despite these studies that advance the knowledge of material's properties of single TRISO layers under reactor operation conditions, the influence of α irradiation on an integrated, multilayer TRISO structure under radiation damage and temperature parameters representative of repository-relevant environments remains unknown.

The literature on γ irradiation of TRISO fuel, is even more scarce than that on α irradiation, as γ-irradiation is mostly recognized as a source of ionization and radiolysis under repository-relevant conditions, and most research focuses on the subsequent UFC corrosion caused by these processes.[23] For nuclear-grade graphite, γ irradiation up to a dose of 87 MGy has been shown to alter the oxidation state of the surface.[24] γ irradiation on 6H-SiC has been reported to decrease

crystallinity and increase amorphization, as well as alter surface chemistry by creating Si–O and O–H functional groups.[25,26] Therefore, the effect of γ irradiation on semi-isotropic IPyC and 3C-SiC as an integrated multilayer TRISO structure under repository-relevant conditions is also an outstanding question in the literature.

Beyond structural and chemical stability, the long-term performance of TRISO fuel is fundamentally governed by the mechanical integrity of its coating layers.[27,28] Radiation-induced defect accumulation can lead to hardening, embrittlement, local stress concentration, and degradation of interlayer cohesion, all of which directly influence coating reliability under service and storage conditions. Even subtle changes in hardness and elastic modulus at the microscale can significantly alter crack initiation and propagation behavior in multilayer ceramic systems. Therefore, mechanical response serves as a sensitive indicator of radiation-driven damage evolution in PyC and SiC layers. Among available techniques, nanoindentation is especially valuable because it enables localized probing of mechanical properties at the scale of individual coating layers, allowing direct correlation between radiation-induced microstructural changes and mechanical performance degradation.[29,30] Understanding these property changes is essential for assessing the ability of TRISO coatings to maintain structural integrity and continue acting as an effective barrier against radionuclide release over long timescales.

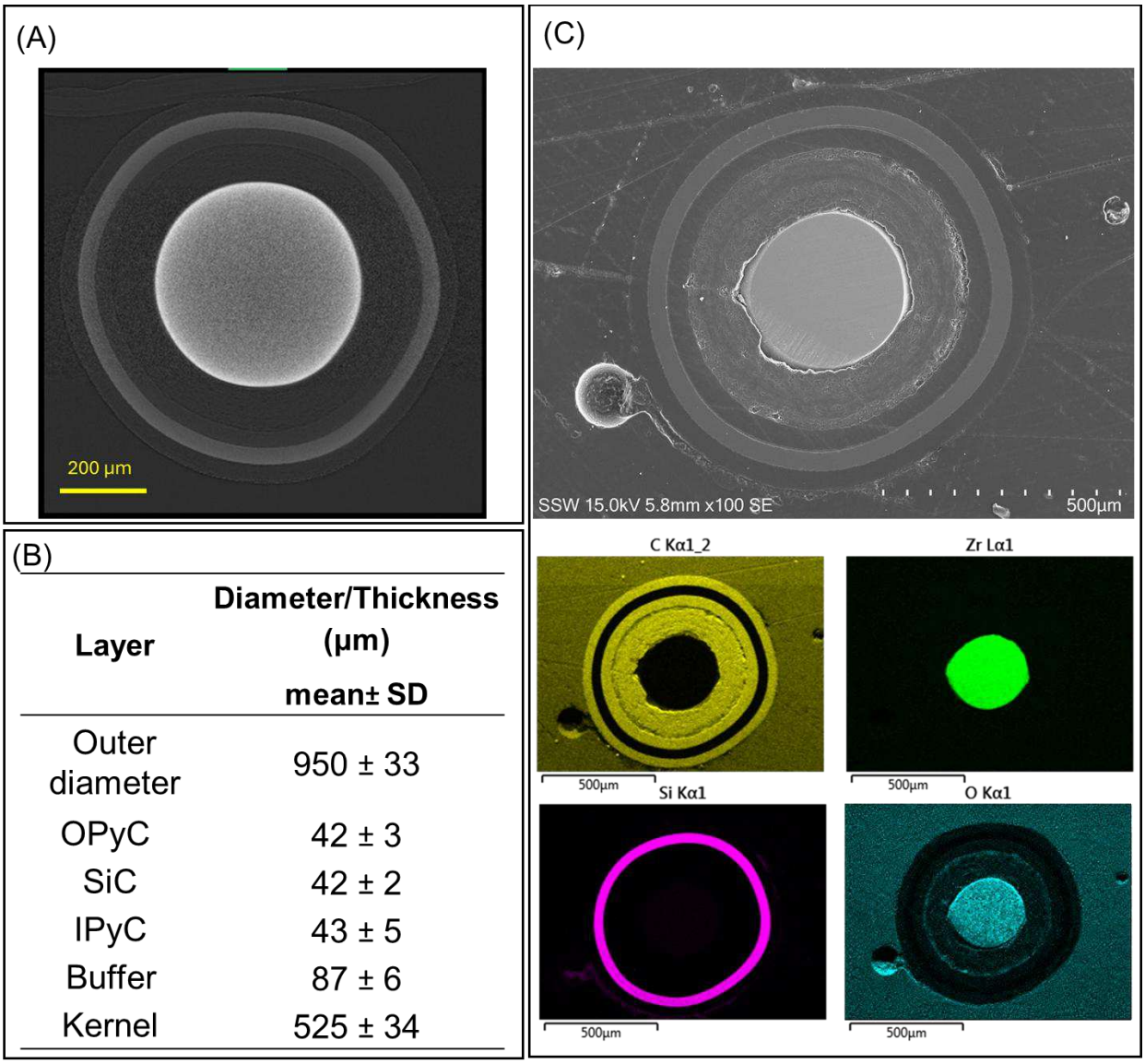
Overall, a key gap exists in understanding how radiation affects TRISO fuel as a coupled multilayer system rather than as isolated components. In particular, the combined evolution of PyC and SiC layers under radiation exposure and its implications for coating stability and radionuclide retention are not well established. This work addresses this gap by investigating radiation-induced changes in surrogate TRISO particles under conditions relevant to long-term disposal environments. He and Au implantations were performed at room temperature, and Au implantation at 100 °C was performed to mimic expected DGR temperatures. [31] Structural and chemical evolution of the coating layers was examined in relation to radiation exposure, and the resulting changes in mechanical response were evaluated to better understand possible degradation affecting long-term fuel integrity.

Results and discussion

TRISO Particle Layer Chemical and Thickness Characterization

X-ray micro-computed tomography (μ-CT, also commonly known as XCT) was conducted on five of the as-received TRISO surrogate particles, and the thicknesses and other characteristics of each constituent layer were determined. Figure 2A shows a central slice from a reconstructed image, in which the different constituent layers can be distinguished by their grayscale contrast, which relates to density variations. The dimensional measurement for each layer is reported as a table in Figure 2B. The measured dimensions are generally consistent with the typical dimensions reported for TRISO and TRISO surrogate particles in the literature.[32,33] Previous studies have commonly reported kernel diameters in the range of approximately 350–500 μm and coating layer thicknesses of about 30–45 μm for IPyC, SiC, and OPyC, while the buffer layer is usually thicker, around 90–100 μm. For example, AGR-1 TRISO particles were reported to have a 350 μm UCO kernel, a 100 μm buffer, a 40 μm IPyC layer, a 35 μm SiC layer, and a 40 μm OPyC layer.[32] In another μ-CT study on surrogate TRISO particles, the kernel diameter was approximately 514 μm, with buffer, IPyC, SiC, and OPyC thicknesses of about 94, 31, 41, and 78 μm, respectively. [33] Therefore, the layer thicknesses measured in this study are within the expected range for TRISO-type particles, with the thicker OPyC and larger kernel reflecting the specific surrogate particle design used here.

To examine the elemental composition of the as-received material, cross-sectioned, mounted particles were analyzed by SEM-EDX. Figure 2C shows a representative SEM image together with the corresponding EDX maps. The elemental maps confirmed the primary elements expected in each layer, and no major unexpected impurities were observed.



(B)

Layer	Diameter/Thickness (µm) mean± SD
Outer diameter	950 ± 33
OPyC	42 ± 3
SiC	42 ± 2
IPyC	43 ± 5
Buffer	87 ± 6
Kernel	525 ± 34

Figure 2: (A) Central µ -CT slice of an as-received surrogate TRISO particle showing the constituent layers and (B) their measured average dimensions and associated standard deviations (SD). (C) SEM image and corresponding EDX elemental maps of a cross-sectioned surrogate TRISO particle.

Chemical Characterization of Irradiated TRISO Layers

After exposure to different irradiation conditions, each layer of the TRISO particles was characterized using Raman spectroscopy to compare with the data collected for unirradiated specimens (Ref). Four types of specimens were analyzed: γ-irradiated specimens (Gamma), specimens that underwent He implantation at room temperature (He-RT), specimens that

underwent Au implantation at room temperature (Au-RT), and specimens that underwent Au implantation at 100 °C (Au-100 °C). Raman spectra collected from the SiC and PyC layers of unirradiated and γ-irradiated TRISO particles are presented in Figure 3A and B, respectively. The inset in Figure 3A shows the optical image acquired during Raman analysis of the cross-sectioned TRISO particle, with the laser positioned on a single layer. The image illustrates the visible contrast between the coating layers, which allowed the target layer to be selected for Raman measurement.

The SiC layer of both the Ref and Gamma specimens exhibited the characteristic transverse optical (TO) and longitudinal optical (LO) Raman modes at approximately 796 and 973 cm^{-1}, respectively (Figure 3A), confirming the crystalline nature of the SiC coating. Raman measurements were performed on all PyC layers, including the buffer, IPyC, and OPyC. Since all three layers exhibited a similar response to ion implantation, only the IPyC data are shown here and the rest are included in supplementary information, Figure S2. As seen in Figure 3B, the Ref-IPyC exhibited the characteristic first-order D and G bands at approximately 1350 and 1605 cm^{-1}, together with their second-order features in the 2700-3100 cm^{-1} region. As shown in Figure 3A, γ irradiation did not produce any noticeable change in the Raman vibrational features of the PyC and SiC layers. The absence of noticeable changes in the Raman spectra indicates that γ irradiation did not cause substantial damage to the carbon or Si–C bonding in the barrier layers. This was expected because the γ irradiation was performed under vacuum, where the formation of radiolysis products is limited and fewer reactive species were likely available to interact with the PyC and SiC layers.

Figure 3C compares the Ref with different ion implanted TRISO particles. In the SiC layer, after the ion implantation, the characteristic SiC phonon modes are no longer observed and the spectra become featureless in this region, indicating severe lattice disorder and likely amorphization of the implanted near surface SiC. This interpretation is consistent with prior ion-irradiation studies on bulk SiC, where irradiation damage caused weakening and eventual disappearance of the original Si–C vibrational modes, together with the formation of an amorphous SiC layer.[34,35] In addition, the Au-100 °C specimen did not show recovery of the TO and LO peaks, indicating that implantation at this temperature was also not sufficient to induce noticeable annealing or restore the crystalline SiC structure.

In the IPyC layers shown in Figure 3D, after ion implantation, regardless of the temperature or ion used, the distinct D and G graphitic features became broadened and less resolved and the second-order bands in the 2700-3100 cm^{-1} region disappeared. The resulting spectra resemble those typically reported for highly disordered or diamond-like amorphous carbon,[36] indicating that both He and Au implantation substantially disrupt the original graphitic ordering of the IPyC structure. This finding is important because it indicates that irradiation-induced structural degradation in SiC is not significantly annealed at 100 °C. Therefore, any material response governed by this transition from a crystalline to a more amorphous structure, including changes in mechanical properties or chemical reactivity, may persist under this temperature condition.

It should be noted that these Raman observations reflect the near-surface (on the order of a few micrometers) region affected by implantation on the cross-sectioned specimens rather than the full thickness of the coating layers. Based on the SRIM calculations and the corresponding vacancy profiles shown in Figure S1, the implantation-induced damage is expected to extend to a depth of approximately 1.5 μm in the SiC layer and about 2.5 μm in the IPyC layer. Since Raman spectroscopy probes the surface and near-surface volume of the material, the structural changes discussed here are attributed specifically to the implanted near-surface region.

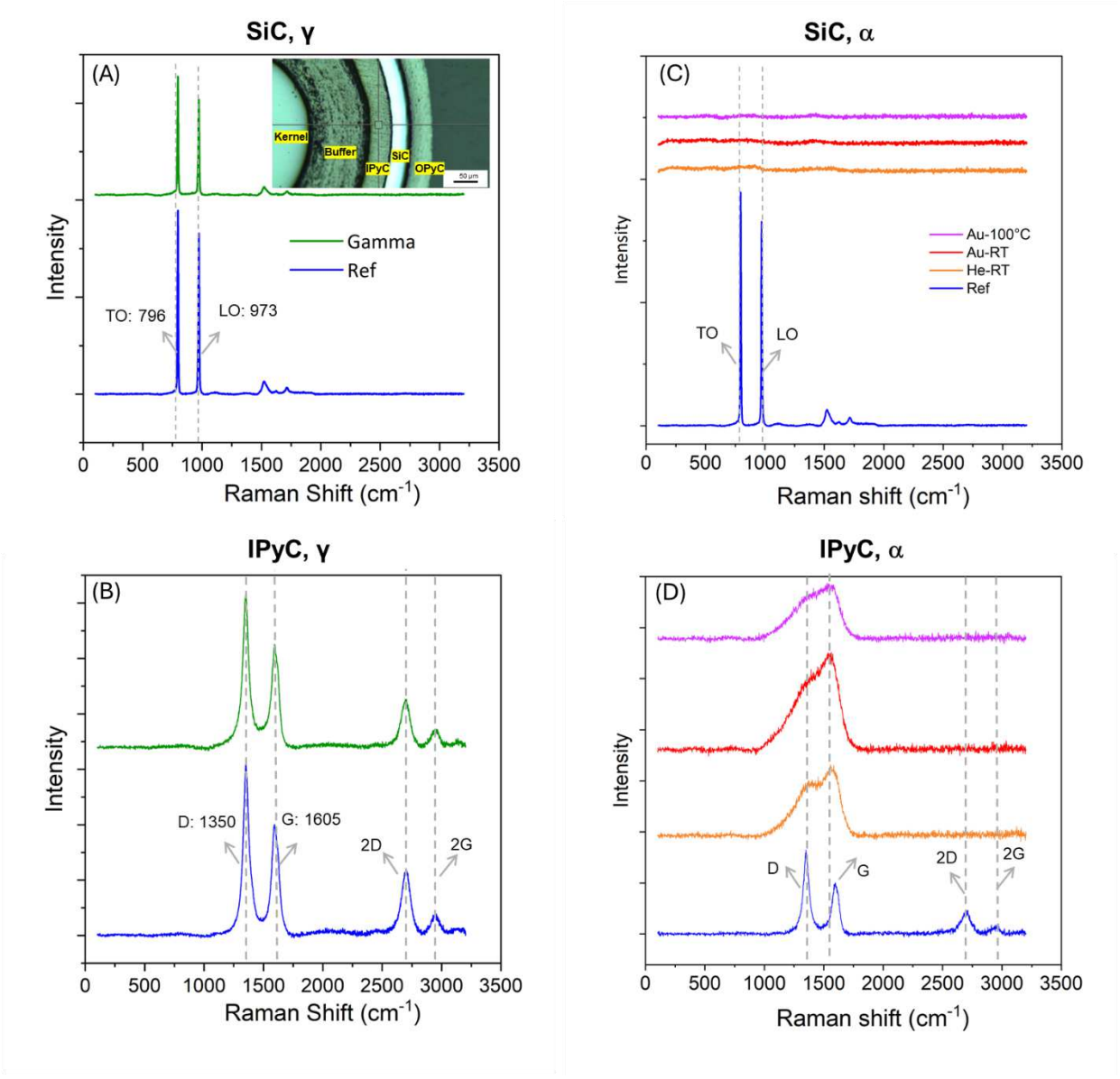


Figure 3 Comparing Raman spectra of IPyC and SiC layers for different irradiated specimens: (A) γ-irradiated SiC, (B) γ-irradiated IPyC, (C) ion implanted for unirradiated (Ref), He implanted at room temperature (He-RT), Au implanted at room temperature (Au-RT), Au implanted at 100°C (Au-100°C), and γ-irradiated (Gamma) for (C) SiC and (D) IPyC layers. The inset of panel (A) shows the cross-sectioned TRISO particle under a Raman microscope.

To further analyze the changes in IPyC, the first-order Raman region was deconvoluted using the fitting approach reported by Sadezky et al.,[37] consisting of four Lorentzian bands assigned to the G, D1, D2, and D4 vibrational bands, together with a Gaussian band assigned to the D3 band, which was identified as the most suitable combination for disordered carbon materials. In this framework, the D3 band is associated with amorphous carbon, whereas the D4 band is commonly

related to disordered graphitic lattices and, in some cases, ionic impurities.[38] The fittings shown in Figure 4A and B confirm that there were no major detectable changes caused by γ irradiation. Figure 4C to E show that ion implantation leads to a clear increase in the D3 and D4 contributions relative to the unirradiated condition, consistent with increased structural disorder and amorphization of the PyC. Overall, the fitting results show that both He and Au implantation drive the PyC away from its original graphitic structure toward a more disordered carbon state. In addition, implantation at 100 °C does not appear to restore the Raman response toward that of the unirradiated material, suggesting that this temperature is insufficient to produce significant annealing of the implantation-induced damage, again emphasizing that any associated changes in material behavior are also likely to persist.

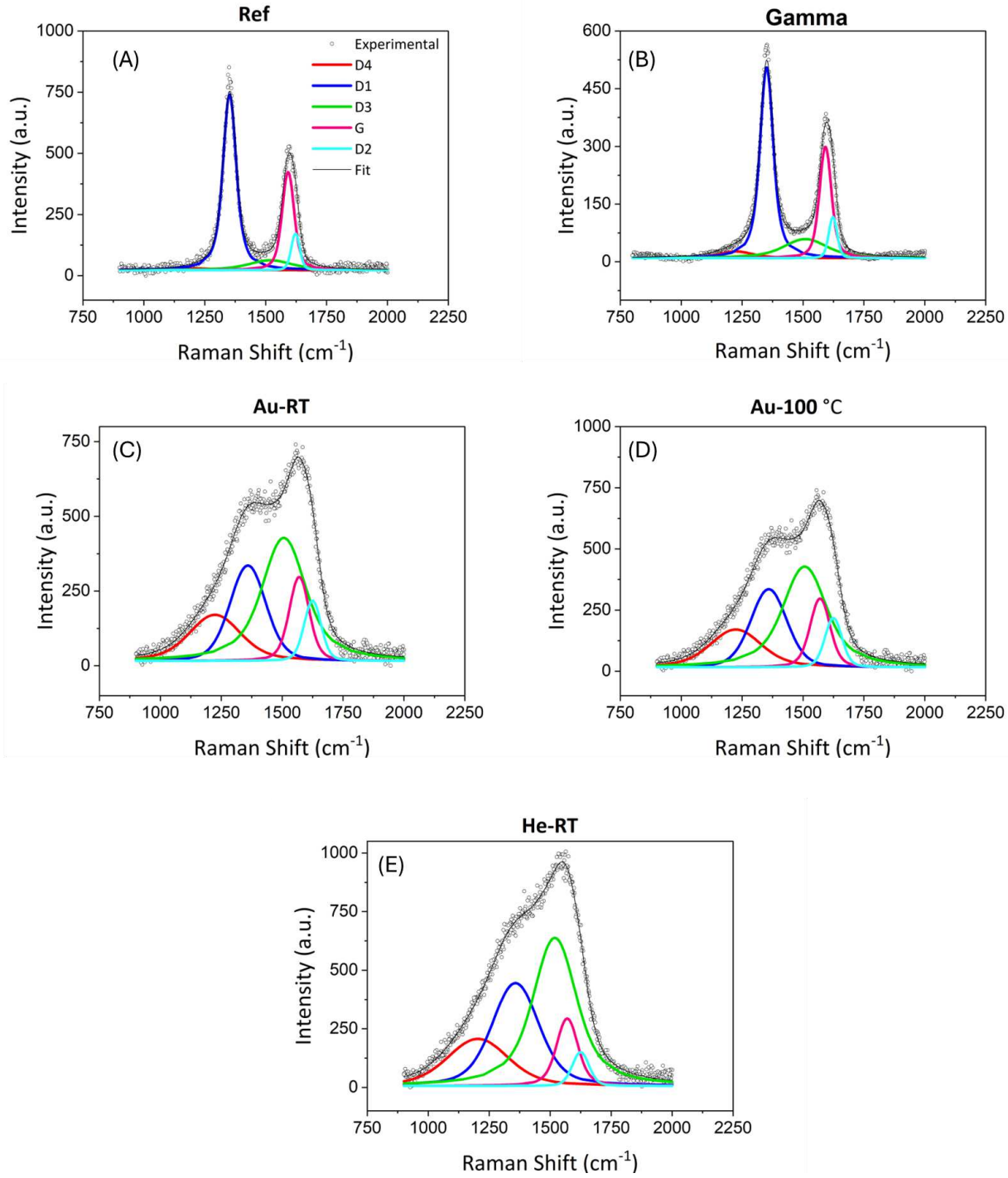


Figure 4: Deconvolution of the first-order Raman region of PyC in different specimens: (A) unirradiated; (B) γ-irradiated; (C) Au implanted at room temperature; (D) Au implanted at 100 °C; and (E) He implanted at room temperature.

Nano Mechanical Response of Irradiated TRISO Layers

Nanoindentation measurements were performed on the SiC and IPyC layers of all five groups of specimens, including the control unirradiated specimen (Ref). These measurements were conducted to evaluate the influence of irradiation type and implantation temperature on the local mechanical response of the TRISO coating layers. Representative load-displacement curves, SEM images of the residual indents, and measured properties are shown for the SiC and IPyC layers in Figure 5 and 6, respectively, while the extracted nanoindentation parameters are summarized in Table S3.

The SiC layer exhibited pronounced irradiation-dependent changes in mechanical behavior. The unirradiated SiC showed a hardness of 30.66 ± 0.06 GPa and an elastic modulus of 330 ± 20 GPa. After γ irradiation, both properties decreased significantly, to 21.62 ± 0.03 GPa and 233 ± 7 GPa, respectively, as shown in Figure 5C and 4D. This softening is clearly reflected in the load-displacement curves of Figure 5A. The γ-irradiated specimen exhibited the largest maximum penetration depth (h_{max} = 1040 ± 50 nm) among all conditions, as can be observed in Figure 5E. The larger displacement under the same peak load, together with an increased residual depth after unloading (h_f = 220 ± 20 nm, Figure 5F), indicates a softer mechanical response and enhanced plastic deformation. Consistent with this behavior, the SEM image of the residual indent appears larger and less sharply defined than those of the other conditions, including specimen Ref, as shown in Figure 5B.

The γ-irradiated IPyC layer exhibited trends broadly similar to those observed for Gamma-SiC, although the absolute values were considerably lower because of the inherently softer carbonaceous structure, as shown in Figure 6. The unirradiated IPyC exhibited a hardness of 2.22 ± 0.08 GPa and an elastic modulus of 11.0 ± 0.1 GPa, which are presented in Figure 6C and 5D. γ irradiation reduced the hardness to 1.66 ± 0.03 GPa and the elastic modulus to 8.9 ± 0.2 GPa, as seen in Figure 6C and 5D. This softening was accompanied by an increase in maximum penetration depth from 1530 ± 10 nm in the reference condition to 1720 ± 20 nm, the highest value among all IPyC specimens, which is shown in Figure 6E. The corresponding load-displacement curve in Figure 6A exhibited a larger displacement under the same applied load, confirming reduced resistance to deformation. Figure 6B shows a representative SEM image of an indent formed on the IPyC layer. Unlike the SiC layer, where indents were clearly visible after

nanoindentation, the indents on the IPyC layer were difficult to identify. Therefore, only one representative IPyC indent is shown for all specimens. This difficulty was likely due to the more elastic response of the IPyC layer, which led to partial or full recovery of the indent after unloading. In addition, the relatively low contrast and non-uniform surface of the IPyC layer made it difficult to locate the indents in most specimens.

Ion implantation resulted in a different nanomechanical response compared with γ irradiation. Helium implantation induced significant hardening of the SiC layer. Hardness increased to 34.03 ± 0.05 GPa, and the elastic modulus increased to 479 ± 6 GPa. This increased mechanical resistance was accompanied by the lowest maximum indentation depth among all specimens ($h_{max} = 597 \pm 8$ nm) and the smallest residual depth ($h_f = 130 \pm 12$ nm), indicating reduced plastic deformation and enhanced elastic recovery. The steeper unloading segment of the load-displacement curve further confirms the higher stiffness of the He-implanted material.

A distinctly different response was observed for Au implantation. At room temperature, Au implantation reduced the hardness to 17.98 ± 0.01 GPa—even lower than that of the γ-irradiated specimen—while the elastic modulus remained close to the reference value (257 ± 9 GPa). Correspondingly, the maximum penetration depth increased to 910 ± 20 nm, indicating substantial softening of the near-surface region. However, when Au implantation was performed at 100 °C, the mechanical response changed dramatically. The hardness increased to 40.97 ± 0.06 GPa—the highest value measured in this study—and the elastic modulus rose to 520 ± 30 GPa. The indentation depth decreased to 730 ± 30 nm, demonstrating strong irradiation-induced hardening. These results highlight that implantation temperature plays a critical role in determining the final defect structure and mechanical response of the SiC layer.

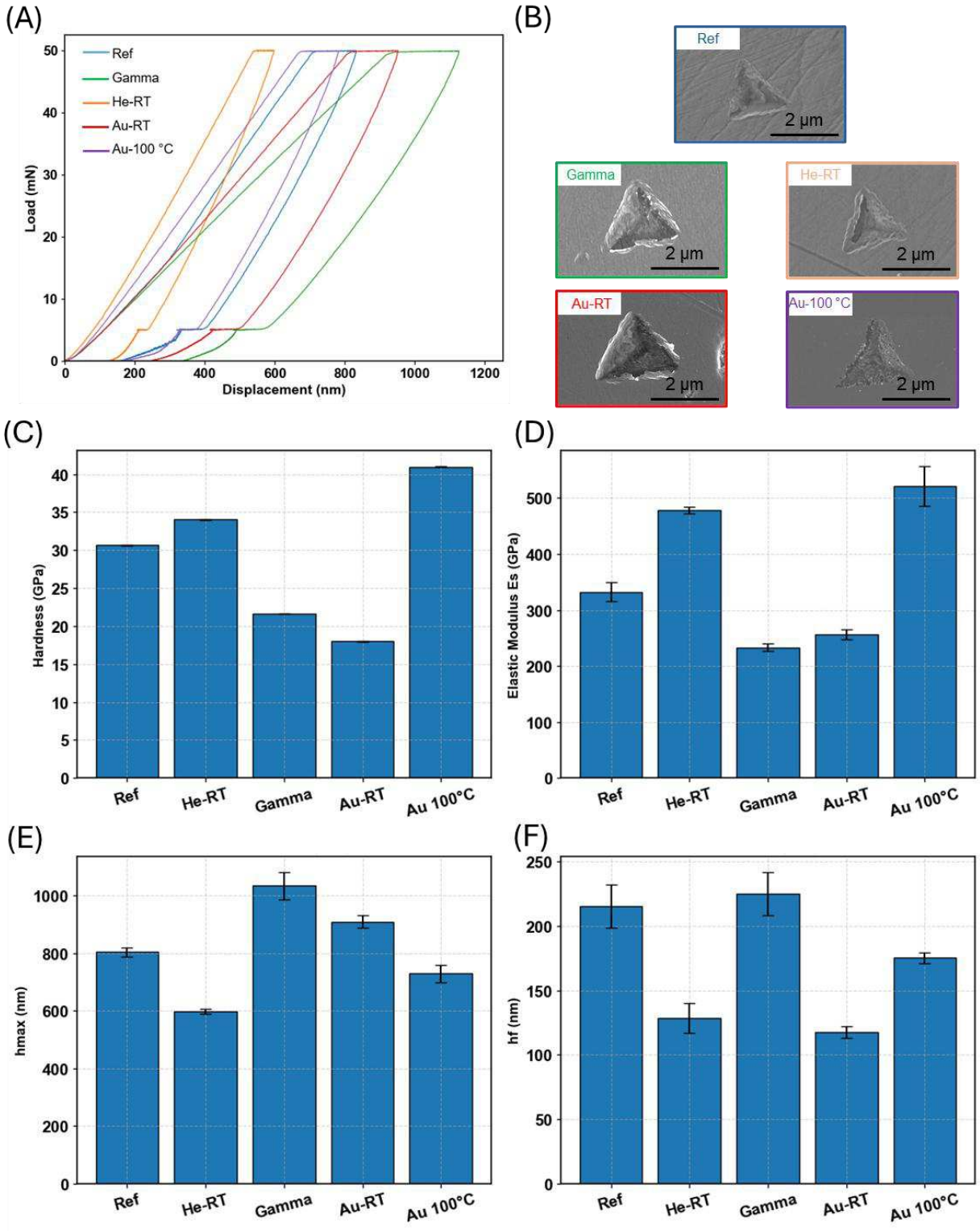


Figure 5: Nanoindentation parameters for SiC layer in different specimens. (A) load-displacement curves, (B) SEM micrographs of individual specimens, (C) hardness, (D) elastic modulus, (E) maximum penetration depth (h_{max}), and (F) residual depth after unloading (h_f).

In the PyC layer, He implantation again produced the strongest hardening response. The hardness increased to 3.6 ± 0.1 GPa, while the elastic modulus increased to 19.7 ± 0.4 GPa, as illustrated in Figure 6C and 5D. Simultaneously, the maximum penetration depth decreased to 1164 ± 6 nm (Figure 6E), indicating a substantial increase in resistance to indentation. Au implantation also increased the hardness and modulus relative to the reference condition. The Au-25 °C specimen exhibited a hardness of 2.4 ± 0.2 GPa and an elastic modulus of 14.3 ± 0.7 GPa, while the Au-100 °C specimen reached 3.02 ± 0.04 GPa and 17.8 ± 0.5 GPa, respectively (Figure 6C and 5D). These results indicate that both He and Au implantation increased the mechanical integrity of the IPyC layer, although the strengthening effect was more pronounced for He implantation.

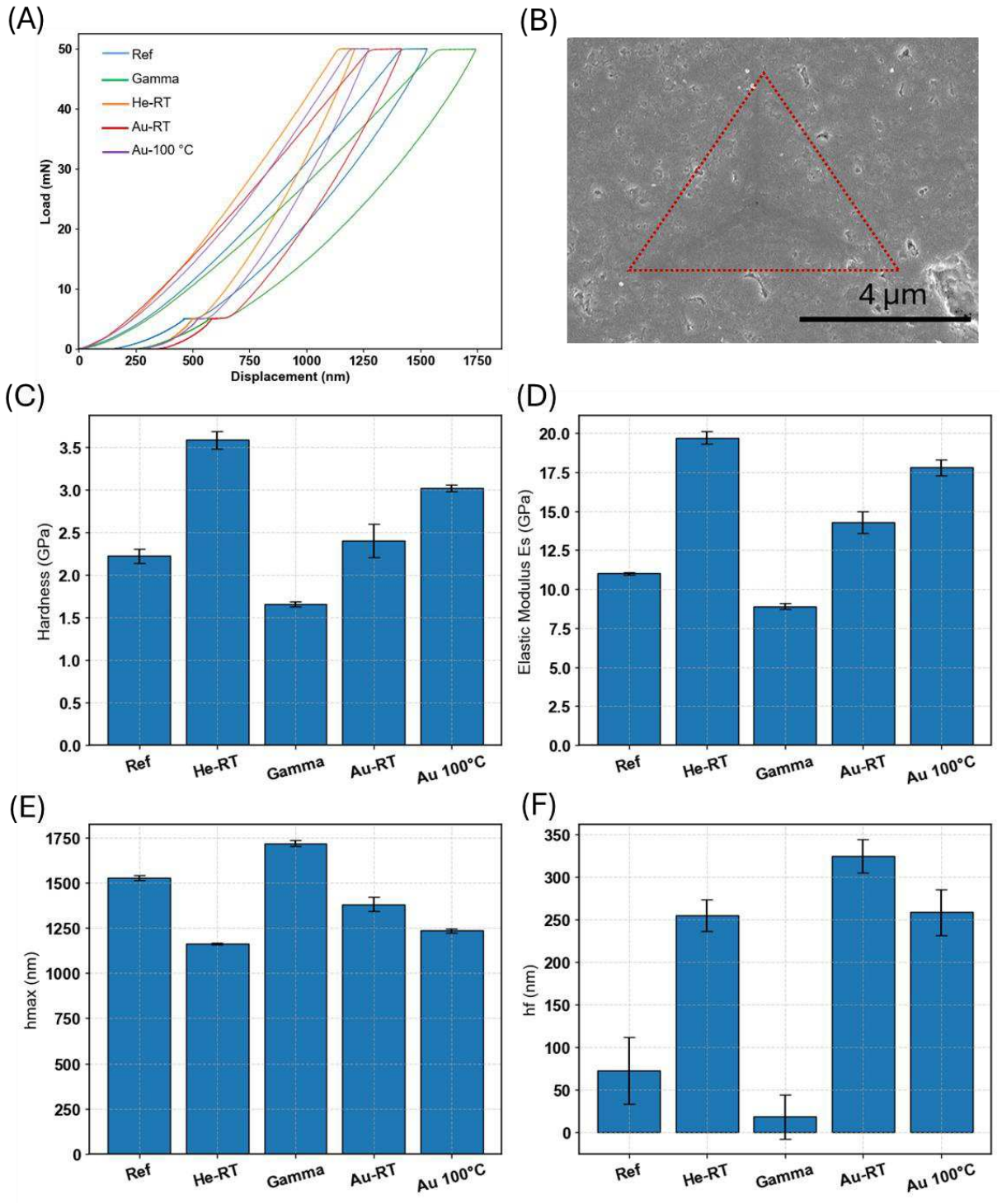


Figure 6: Nanoindentation parameters for the IPyC layer in the different specimens. (A) load-displacement curves, (B) SEM micrograph of a representative specimen (dashed triangle highlights the indent region), (C) hardness, (D) elastic modulus, (E) maximum penetration depth (h_{max}), and (F) residual depth after unloading (h_f).

To better compare the hardness response of the two coating layers, the hardness values for SiC and IPyC under different irradiation conditions are shown side by side in Figure 7 The trends observed in the nanoindentation parameters reveal two distinct irradiation responses. γ irradiation consistently reduced hardness, modulus, and stiffness while increasing indentation depth in both SiC and IPyC, indicating irradiation-induced softening. In contrast, ion implantation generally increased hardness and elastic modulus, particularly for He implantation and Au implantation at elevated temperature.

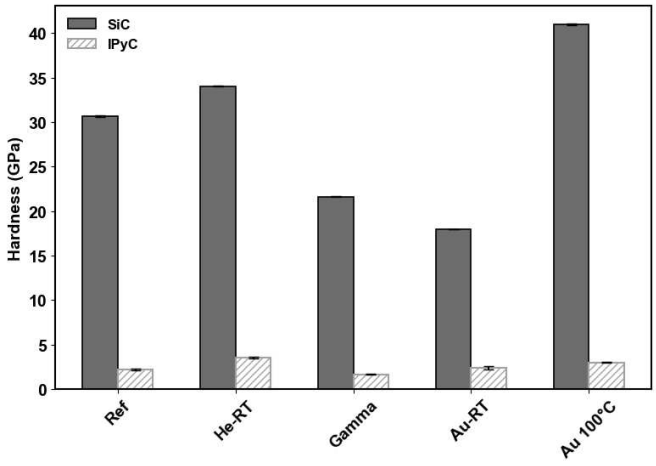


Figure 7: Comparison of SiC and IPyC hardness after treatment under different irradiation conditions.

Changes in hardness after γ irradiation have been reported previously for some materials, but not specifically for the SiC and PyC layers of TRISO particles. In general, even for other systems, fundamental studies on the influence of γ radiation on mechanical property evolution remain limited. For example, $Sn_3Ag_{0.5}Cu$ solder joints showed a non-monotonic change in nanoindentation hardness with increasing γ dose up to 720 kGy, with an initial increase, followed by a decrease, and then further increase. [39] While an oxide-based waste system containing $LiNbO_3$, CaO, and PbO showed a slight decrease in micro-Vickers hardness with increasing γ dose up to 40 kGy. [40] In these cases, changes in hardness have been associated with irradiation-induced atomic-scale defects, including point defects and vacancies, which can affect the local bonding structure and mechanical response. [41] Therefore, the softening observed after γ irradiation in the present study may be related to subtle point defect formation or bond-level disorder. These changes may not be sufficiently extensive to produce clear changes in the Raman spectra, but they can still reduce the local resistance to indentation.

In contrast, ion implantation produced a different mechanical response, with hardening observed in most implanted SiC and IPyC specimens. For SiC, the TO and LO modes disappeared from the Raman spectra after implantation, indicating severe disorder and likely near-surface amorphization. Previous studies on ion irradiated SiC have shown that the mechanical response depends strongly on the damage level. Tromas et al. [42] reported that irradiation-induced hardening can occur at lower damage levels, whereas complete amorphization is associated with a strong decrease in hardness. Similarly, Li et al. [43] showed that hardening is observed when He-implanted SiC is not fully amorphized, and He et al. [44] reported dose-dependent hardening, with the maximum hardening occurring at an intermediate damage level rather than after severe disordering. Taken together, these studies suggest that the mechanical response of irradiated SiC reflects a balance between defect-induced hardening and bond damage/amorphization. In the present study, the hardening observed after He implantation and Au implantation at 100 °C may therefore be attributed to the formation of a highly damaged near-surface region, where defect accumulation, implanted species, and possible residual compressive stresses increase resistance to localized deformation.

The lower SiC hardness observed after Au implantation at room temperature may indicate that, under this condition, bond damage and amorphization were more dominant than defect-induced hardening. Wallace et al.[45] experimentally demonstrated defect relaxation in ion-irradiated 3C-SiC on a millisecond timescale at 100 °C. This relaxation was attributed to point-defect migration, interaction, and recombination. Therefore, implantation at 100 °C may have promoted partial recovery of irradiation-induced defects, although the temperature was not sufficient to restore the original crystalline structure.

As described in the experimental section, full TRISO particles were exposed to γ-radiation without being cross-sectioned. This made it possible to perform non-destructive μ-CT on the full TRISO particles before and after irradiation to examine any possible internal dimensional or microstructural changes within the same particle. For this group of specimens, sample preparation and cross-sectioning for microscopic characterization and nano-indentations were done after irradiation. Figure 8 compares unirradiated and γ-irradiated particles using optical microscopy, SEM, and μ-CT.

From the optical images in Figure 8, differences in surface features are evident, despite the fact that the same polishing procedure was used for both. The difference is more noticeable in the buffer layer, where the unirradiated specimen appeared more porous, and the gap between the kernel and buffer appeared larger. In contrast, the γ-irradiated particle showed an apparently denser buffer region, with minimal gaps observed. A closer examination of the same region by SEM, with the stage tilted by 45° to better reveal the surface topography, confirmed this observation. For the γ-irradiated specimen, the gap appeared to be filled, whereas in the unirradiated specimen the gap remains more clearly visible. However, the reconstructed μ-CT images of the same particle before and after γ exposure do not show major changes, within the resolution and contrast of the micro-CT settings used, in the buffer porosity or overall internal structure. This suggests that the differences observed in the polished cross-sections likely developed during sample preparation rather than being an original structural change caused during irradiation. Since the polishing method was the same for both specimens, these observations may indicate a difference in the material's response to abrasive polishing before and after γ-irradiation. This is consistent with the nanoindentation results, which showed a softer material after γ irradiation. The denser appearance of the γ-irradiated specimen may therefore be related to increased smearing of the softer material during polishing, leading to partial filling of surface gaps and pores. Although this assessment is qualitative, it provides supporting microscopic evidence consistent with the lower hardness measured by nanoindentation.

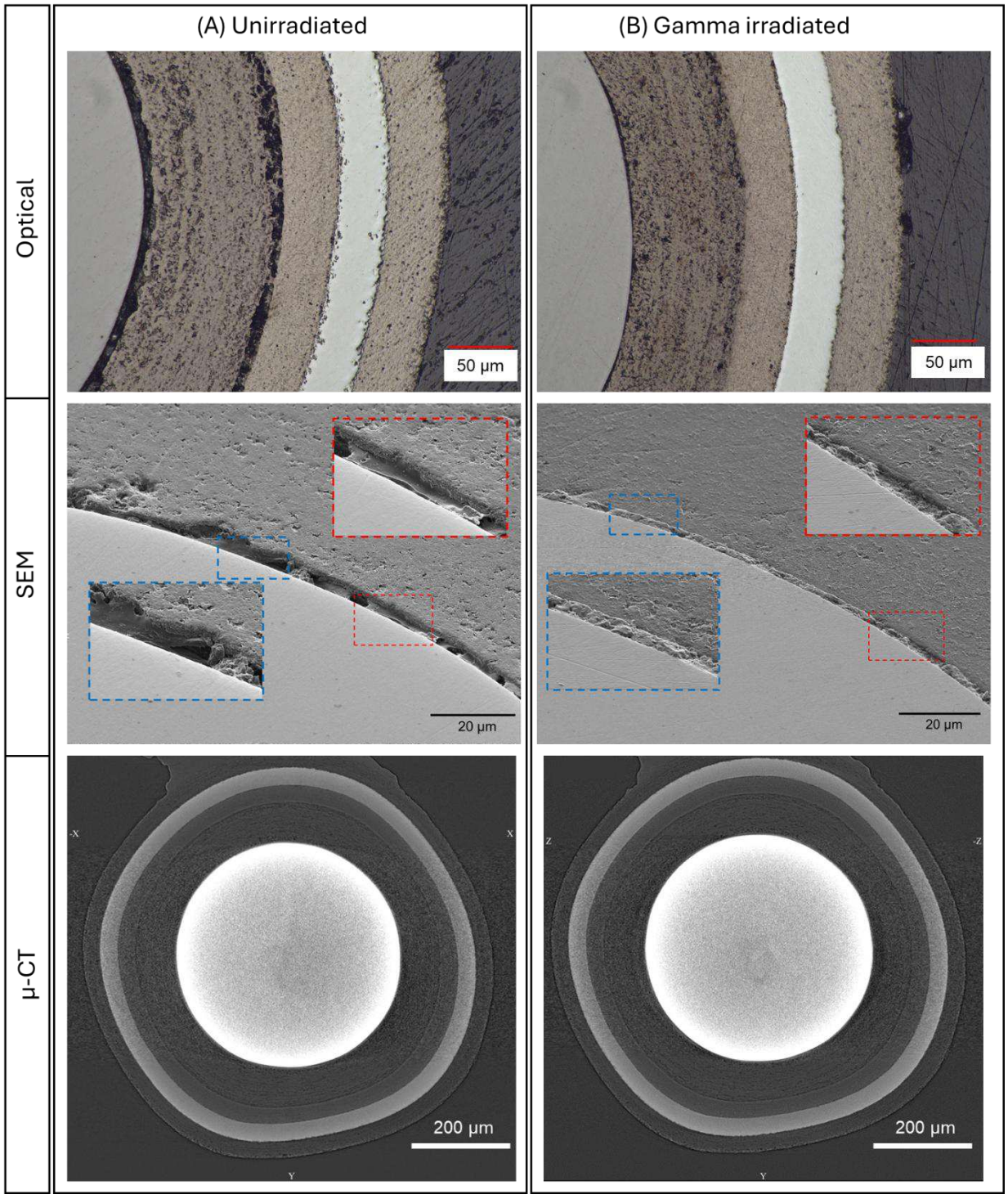


Figure 8: Optical microscopy, SEM, and μ-CT images comparing TRISO particles in the (A) unirradiated and (B) γ-irradiated conditions.

Additionally, the influence of irradiation-induced structural changes on the chemical durability and corrosion resistance of the coating layers may also be important for long-term DGR

performance, but this was not investigated in the present work. From the perspective of TRISO performance in a DGR environment, the softening observed after γ irradiation does not necessarily indicate improved or degraded integrity by itself. Rather, it shows that γ irradiation can modify the local mechanical response of the coating layers. This could influence how the layers respond to mechanical stresses, such as internal gas pressure or externally applied loads in long-term degraded repository scenarios. Softening may improve deformation accommodation, but it may also reduce load-bearing capacity. In contrast, the higher hardness and elastic modulus measured after ion implantation, together with the absence of recovery in the Au-100 °C condition, indicate that implantation-induced damage remained largely unrecovered at 100 °C. Such hardening may reduce deformation tolerance and increase susceptibility to stress-induced cracking. However, to better assess whether these irradiation-induced changes improve or degrade the mechanical integrity of the coating system, additional measurements, particularly fracture toughness or cracking resistance, would be required. Additionally, the influence of irradiation-induced structural changes on the chemical durability and corrosion resistance of the coating layers may also be important for long-term DGR performance, but this was not investigated in the present work.

In summary, this study examined the effects of α and γ radiation on the PyC and SiC layers of surrogate TRISO particles under anticipated DGR-relevant conditions. Ion implantation caused irreversible structural changes in both materials. Raman results showed that PyC evolved toward a more disordered carbon structure, while SiC lost its characteristic TO and LO Raman peaks, indicating severe disorder and likely near-surface amorphization. In both materials, implantation at 100 °C did not produce noticeable recovery. The mechanical response of TRISO coating layers depended strongly on the irradiation type and temperature. In SiC layers, γ irradiation caused softening, helium implantation induced hardening, and Au implantation resulted in a transition from severe softening at room temperature to the highest increase of hardness at 100 °C. γ irradiation also softened the IPyC layer, as shown by the reduced hardness and elastic modulus. The IPyC layer showed similar hardening under helium and gold implantation but no softening, with consistently lower absolute values due to its inherently softer structure. Overall, the results indicate that α radiation-relevant damage has a stronger effect than the investigated γ dose and energies on the structure and mechanical response of TRISO coating layers. These changes may increase the susceptibility of the coating layers to cracking or fracture and are therefore important for understanding the long-term containment performance of TRISO fuel in repository conditions.

Experimental

Materials and Sample Preparation

Surrogate TRISO particles with zirconium oxide kernels were supplied by Standard Nuclear Inc. For cross-sectional analysis, particles were cold-mounted in the EpoFix epoxy system purchased from Struers and then polished to expose all five constituent layers. Polishing was performed using a combination of diamond lapping films (Lee Valley) and diamond suspensions (Struers), down to a final abrasive size of 0.25 μm, to obtain a smooth surface.

Irradiation Experiments

γ radiation experiments were performed using a Nordion GC-220 Excel gamma cell (^{60}Co source, dose rate 574 Gy/h) of the Western University Department of Chemistry. The fully coated particles were placed in the gamma cell for 20 days to achieve total doses of 276 kGy. For the exposure, the particles were placed in a borosilicate glass pipette which was then evacuated and sealed with a flame.

α irradiation experiments were conducted on cross-sectioned TRISO particles. For each irradiation, three particles were mounted and irradiated simultaneously to account for reproducibility of irradiation results for the particle characterization. Ion implantation using a 1.7 MV Tandetron accelerator (High Voltage Engineering Europa) facility at Western University, was performed to reflect the α damage expected under repository-relevant conditions. The target radiation damage of ~1 DPA with multi-energy implantation was selected to represent the expected damage in a DGR after 1000 years.[31] He ions were used to simulate α particles, which consist of two protons and two neutrons. To accelerate the damage process, heavy Au ions were implanted to produce the same number of DPA in a much shorter time. Based on Stopping and Range of Ions in Matter (SRIM) calculations,[46] two sets of implantation experiments using He and Au ions were designed to create a uniform vacancy profile within a depth of ~1.5 to 3 μm across the different layers. Tables S1 and S2 show the energy and dose settings for multi-energy implantation using Au and He ions, respectively, for the investigated PyC and SiC layers. The vacancies, ion range, and straggling distance for each implantation step are included in the tables. For the SRIM calculations, the displacement energies were set to 25 eV and 20 eV for carbon atoms in IPyC and

SiC, respectively, and 41 eV for Si atoms in the SiC lattice.[47,48] The multi-energy implantation for both Au and He resulted in radiation damage of around 1.1 DPA in the SiC layer and 0.35 DPA in the PyC layers. Three separate implantation experiments were done: He implantation at room temperature, Au implantation at room temperature, and Au at 100 °C to mimic expected DGR temperatures.[49]

Characterization of TRISO particles

A Zeiss Xradia 410 Versa μ-CT was used as a non-destructive technique to quantify the thickness of the constituent layers and to examine possible dimensional changes following γ irradiation. A Kapton tube with an inner diameter of 1.2 mm and a wall thickness of 38 μm was used to immobilize the TRISO particles. For all scans, no filter was used (air), and the operating conditions were 40 kV, 10 W, 142 μA, 20× optical magnification, an exposure time of 45 s, and scans were done over 180° with two-frame averaging. In order to assess the differences between individual particles, dimensional analyses were performed on five different particles. The measurements were done on the same plane for each particle. For each layer, three manual measurements were taken using the ruler tool in ORS Dragonfly Pro software, and the average values and standard deviations were calculated.

Scanning electron microscopy (SEM) was performed in secondary electron mode at an accelerating voltage of 3 kV using a LEO/Zeiss 1530XB SEM (Oberkochen, Germany) and a Hitachi SU3900 SEM. Energy-dispersive X-ray spectroscopy (EDX) analysis was performed using a Hitachi SU3900 equipped with a Oxford ULTIM Max 65 SDD detector at an accelerating voltage of 15 kV.

Raman spectroscopy (Renishaw InVia Reflex Raman Spectrometer) with monochromic laser wavelength of 514 nm and a 50× objective was used to collect spectra over a Raman shift from 100 to 3200 cm^{-1}.

Nanoindentation Measurements

Nanoindentation experiments were conducted using an Alemnis instrument equipped with a Berkovich indenter tip to evaluate the mechanical response of the irradiated layers. Tests were performed at a loading rate of 10 mN s^{-1} up to a maximum load of 50 mN. The maximum load

was held for 5 s prior to unloading to minimize creep effects, followed by unloading at the same rate of 10 mN s^{-1}. Each indentation cycle lasted 15 s, and a 30 s thermal drift correction measurement was conducted after each indentation.

The hardness and elastic modulus were determined from the load–displacement curves using the standard Oliver-Pharr method.[50]

Hardness (H) was calculated using the Oliver-Pharr method as:

$$\mathrm{H} = \frac{F_{max}}{\mathrm{A_c}} \tag{1}$$

where F_{max} is the peak load and A_c is the projected contact area, obtained using the contact depth h_c and an empirically derived polynomial area function[51]:

$$\mathrm{A_c}(\mathrm{h}_c) = 24.5\mathrm{h}_c^2 + \mathrm{C_1 h}_c + \mathrm{C_2 h}_c^{\frac{1}{2}} + \mathrm{C_3 h}_c^{\frac{1}{4}} + \cdots + \mathrm{C_8 h}_c^{\frac{1}{128}} \tag{2}$$

The contact stiffness was extracted from the initial unloading slope to determine the reduced modulus E_r:

$$E_r = \frac{1}{2}\frac{dp}{dh}\frac{\sqrt{\pi}}{\sqrt{A_c}} \tag{3}$$

$$\frac{1}{E_r} = \frac{(1-\nu^2)}{E} + \frac{\left(1-\nu'^2\right)}{E'} \tag{4}$$

Here, E and ν are the elastic modulus and Poisson's ratio of 3C-SiC (ν = 0.17), and E′ = 1140 GPa and ν′ = 0.07 are the indenter properties[52]. Calibration tests on fused silica (standard values: E_r = 69.7 GPa, H = 9.65 GPa) were used to correct for machine compliance and tip rounding [50,53]. Nanoindentation tests for each sample group were performed on three different particles. For each layer, at least five measurements were collected. The indents were placed at a similar radial distance from the particle center and near the middle of the SiC and IPyC layer thicknesses. The reported errors represent the standard deviation of the measurements.

Acknowledgements:

The authors acknowledge the support of Natural Resources Canada (Enabling Small Modular Reactors Program). The authors thank Surface Science Western for access to the Raman facilities

and SEM/EDX. The authors acknowledge the Nanofabrication Laboratory for access to the SEM/EDX. The authors also acknowledge Multi-Scale Deformation Lab at Western Engineering for access to the Alemnis instrument for nanoindentations.

References:

1. Alwaeli, M. & Mannheim, V. Investigation into the Current State of Nuclear Energy and Nuclear Waste Management—A State-of-the-Art Review. *Energies* **15**, 4275 (2022).
2. International Atomic Energy Agency. *Small Modular Reactors: Advances in SMR Developments 2024*. (IAEA, Vienna, 2024).
3. L'Her, G. F., Kemp, R. S., Bazilian, M. D. & Deinert, M. R. Potential for Small and Micro Modular Reactors to Electrify Developing Regions. *Nat. Energy* **9**, 725–734 (2024).
4. Locatelli, G., Bingham, C. & Mancini, M. Small Modular Reactors: A Comprehensive Overview of Their Economics and Strategic Aspects. *Prog. Nucl. Energy* **73**, 75–85 (2014).
5. Dong, Z. *et al.* Testing the Feasibility of Multi-Modular Design in an HTR-PM Nuclear Plant. *Nat. Commun.* **16**, 2778 (2025).
6. Iaroslav O. Bykh & Inna V. Yurina. Regulatory control features and principles for a land-based RITM-200N SNPP project. (2023).
7. International Atomic Energy Agency. *Advances in Small Modular Reactor Technology Developments: A Supplement to IAEA Advanced Reactor Information System (ARIS), 2018 Edition.* (IAEA, Austria, 2018).
8. Powers, J. J. & Wirth, B. D. A review of TRISO fuel performance models. *J. Nucl. Mater.* **405**, 74–82 (2010).
9. Price, M. S. T. The Dragon Project Origins, Achievements and Legacies. *Nucl. Eng. Des.* **251**, 60–68 (2012).
10. Collin, B. P. *AGR-1 Irradiation Test Final As-Run Report*. (2014).

11. Dungan, K., Gregg, R. W. H., Morris, K., Livens, F. R. & Butler, G. Assessment of the Disposability of Radioactive Waste Inventories for a Range of Nuclear Fuel Cycles: Inventory and Evolution Over Time. *Energy* **221**, 119826 (2021).
12. Apted, M. J. & Ahn, J. *Geological Repository Systems for Safe Disposal of Spent Nuclear Fuels and Radioactive Waste*. (Woodhead Publishing, 2017).
13. Umadevi, K. & Mandal, D. Performance of Radio-iodine Discharge Control Methods of Nuclear Reprocessing Plants. *J. Environ. Radioact.* **234**, 106623 (2021).
14. Algora, A., Tain, J. L., Rubio, B., Fallot, M. & Gelletly, W. Beta-decay studies for applied and basic nuclear physics. *Eur. Phys. J. A* **57**, 85 (2021).
15. Rodriguez, D. C. *et al.* Measurement and Analysis of Gamma-rays Emitted from Spent Nuclear Fuel above 3 MeV. *Appl. Radiat. Isot.* **82**, 181–187 (2013).
16. Hunn, J. D. *et al.* Detection and Analysis of Particles with Failed SiC in AGR-1 Fuel Compacts. *Nucl. Eng. Des.* **306**, 36–46 (2016).
17. He, X. *et al.* Direct Characterization of Ion Implanted Pyrolytic Carbon Coatings Deposited from Natural Gas. *Carbon* **68**, 95–103 (2014).
18. Krajewska, Z. M. *et al.* The Influence of the Ion Implantation on the Degradation Level of the Coated Particles of Nuclear Fuel Samples. *Coatings* **13**, 556 (2023).
19. ASTM E521-16 Standard Practice for Investigating the Effects of Neutron Radiation Damage Using Charged-Particle Irradiation. (2016).
20. Krajewska, Z. M., Górkiewicz, M. & Gudowski, W. Fluence Calculations for the TRISO Particle Fuel Ion Implantation Experiment. *Prog. Nucl. Energy* **162**, 104786 (2023).
21. Snead, L. L. & Hay, J. C. Neutron Irradiation Induced Amorphization of Silicon Carbide. *J. Nucl. Mater.* **273**, 213–220 (1999).

22. Daghbouj, N. *et al.* Microstructural Evolution of Helium-irradiated 6H–SiC Subjected to Different Irradiation Conditions and Annealing Temperatures: A Multiple Characterization Study. *Acta Mater.* **181**, 160–172 (2019).
23. Skotar, T. *et al.* In Situ Monitoring of Hypochlorite Decay under Radiation Using Differential Pulse Voltammetry. *ACS Electrochem.* https://doi.org/10.1021/acselectrochem.5c00338 (2026) doi:10.1021/acselectrochem.5c00338.
24. Goodwin, C., Barkatt, A. & Al-Sheikhly, M. On the Mechanism of the Interactions of Neutrons and Gamma Radiation with Nuclear Graphite—Implications to HTGRs. *Radiat. Phys. Chem.* **97**, 38–47 (2014).
25. Gaibnazarov, B. B. *et al.* Changes in the Structure and Properties of Silicon Carbide under Gamma Irradiation. *Integr. Ferroelectr.* **237**, 208–215 (2023).
26. Soltanifar, F., Ebrahimibasabi, E. & Shahidi, M. M. Gamma Radiation Effects on SiC nanopowders: Structural, Morphological, Optical and Electrical Evolution. *Ceram. Int.* **51**, 21461–21469 (2025).
27. Hosemann, P. *et al.* Mechanical Characteristics of SiC Coating Layer in TRISO Fuel Particles. *J. Nucl. Mater.* **442**, 133–142 (2013).
28. Montoya, K. I. *et al.* Micromechanical Response of SiC-OPyC Layers in TRISO Fuel Particles. *J. Nucl. Mater.* **606**, 155654 (2025).
29. Frazer, D., Szornel, J., Krumwiede, D. L., Terrani, K. A. & Hosemann, P. Evaluation of the Mechanical Properties of TRISO Particles Using Nanoindentation and Ring Compression Testing. *Exp. Mech.* **57**, 1081–1090 (2017).

30. Leide, A., Hintsala, E., Davies, M., Goddard, D. T. & Liu, D. Micromechanical Properties of TRISO Coatings by in-situ High Temperature Nanoindentation and Microcantilever Fracture. *J. Eur. Ceram. Soc.* **44**, 3112–3120 (2024).
31. Wiss, T. *et al.* Evolution of Spent Nuclear Fuel in Dry Storage Conditions for Millennia and Beyond. *J. Nucl. Mater.* **451**, 198–206 (2014).
32. Bower, G. R., Demkowicz, P. A., Ploger, S. A. & Hunn, J. D. Measurement of Kernel Swelling and Buffer Densification in Irradiated UCO-TRISO Particles. (2017).
33. Lowe, T. *et al.* Microstructural Analysis of TRISO Particles Using Multi-Scale X-ray Computed Tomography. *J. Nucl. Mater.* **461**, 29–36 (2015).
34. Zhang, L. Q. *et al.* Surface Damage on 6H–SiC by Highly-charged Xeq+ Ions Irradiation. *J. Nucl. Mater.* **455**, 704–709 (2014).
35. Pérez-Rodríguez, A. *et al.* Analysis of Ion Beam Induced Damage and Amorphization of 6H-SiC by Raman Scattering. *J. Electron. Mater.* **25**, 541–547 (1996).
36. Chu, P. K. & Li, L. Characterization of Amorphous and Nanocrystalline Carbon Films. *Mater. Chem. Phys.* **96**, 253–277 (2006).
37. Sadezky, A., Muckenhuber, H., Grothe, H., Niessner, R. & Pöschl, U. Raman Microspectroscopy of Soot and Related Carbonaceous Materials: Spectral Analysis and Structural Information. *Carbon* **43**, 1731–1742 (2005).
38. Watanabe, H., Takahashi, K. & Iwaki, M. Structural Dharacterization of Ion Implanted HOPG and Glass-like Carbon by Laser Raman Spectroscopy. *Nucl. Instrum. Methods Phys. Res. Sect. B Beam Interact. Mater. At.* **80–81**, 1489–1493 (1993).
39. Guan, Q. *et al.* Effect of Gamma Irradiation on Microstructural Evolution and Mechanical Properties of Sn3Ag0.5Cu Solder Joints. *J. Mater. Res. Technol.* **24**, 6022–6033 (2023).

40. Abd-Elnaiem, A. M., Saudi, H. A., Zakaly, H. M. H., Issa, S. A. M. & Rashad, M. The Effect of Composition and γ-irradiation on the Vickers Hardness, Structural and Optical Properties of *x*LiNbO3-25CaO-35PbO-(40-*x*) Waste Systems. *Ceram. Int.* **47**, 18751–18760 (2021).

41. Saudi, H. A. Gamma Ray Irradiation Effects on the Mechanical and Chemical Properties of $CuO–Bi_2O_3–SiO_2$ Glasses. *Am. J. Phys. Appl.* **4**, 140–144 (2016).

42. Tromas, C. *et al.* Evolution of Mechanical Properties of SiC Under Helium Implantation. *J. Nucl. Mater.* **373**, 142–149 (2008).

43. Li, B. S. *et al.* Evolution of Strain and Mechanical Properties upon Annealing in He-implanted 6H-SiC. *J. Nucl. Mater.* **455**, 116–121 (2014).

44. He, X. *et al.* A Comparison Study of Mechanical Change and Chemical Disorder in 4H-SiC Irradiated with Si5+ and He2+ at Room Temperature. *Nucl. Instrum. Methods Phys. Res. Sect. B Beam Interact. Mater. At.* **512**, 60–65 (2022).

45. Wallace, J. B., Bayu Aji, L. B., Shao, L. & Kucheyev, S. O. Time Constant of Defect Relaxation in Ion-irradiated 3C-SiC. *Appl. Phys. Lett.* **106**, 202102 (2015).

46. Ziegler, J. F., Ziegler, M. D. & Biersack, J. P. SRIM – The Stopping and Range of Ions in Matter. *Nucl. Instrum. Methods Phys. Res. Sect. B Beam Interact. Mater. At.* **268**, 1818–1823 (2010).

47. Vuković, F., Jean-Marc Leyssale, Philippe Aurel, & Nigel A. Marks. Evolution of Threshold Displacement Energy in Irradiated Graphite. *Phys. Rev. Appl.* **10**, (2018).

48. Li, W. *et al.* Threshold Displacement Energies and Displacement Cascades in 4H-SiC: Molecular Dynamic Simulations. *AIP Adv.* **9**, 055007 (2019).

49. Morris, E. E. & Bauer, T. H. *Modeling of the Repository Behavior of TRISO Fuel*. https://inis.iaea.org/records/aemst-t9g36 (2005).

50. Fischer-Cripps, A. C. *Nanoindentation 2nd Edition*. (Springer, New York, NY, 2004).

51. Oliver, W. C. & Pharr, G. M. An Improved Technique for Determining Hardness and Elastic Modulus Using Load and Displacement Sensing Indentation Experiments. *J. Mater. Res.* **7**, 1564–1583 (1992).

52. Jackson, K. M. Fracture Strength, Elastic Modulus and Poisson's Ratio of Polycrystalline 3C Thin-film Silicon Carbide Found by Microsample Tensile Testing. *Sens. Actuators Phys.* **125**, 34–40 (2005).

53. Beake, B. D. & Smith, J. F. High-Temperature Nanoindentation Testing of Fused Silica and Other Materials. *Philos. Mag. A* **82**, 2179–2186 (2002).

Supplementary Files

This is a list of supplementary files associated with this preprint. Click to download.

- SupportinginformationTRISOnpjmaterialsdegradation2026.pdf